Chinese Chemical Letters 34 (2023) 107831

Contents lists available at ScienceDirect

Chinese Chemical Letters

journal homepage: www.elsevier.com/locate/cclet

Construction of hierarchical nanostructures and NiO nanosheets@nanorods for efficient urea electrooxidation

Qing Li[a,*], Xiaotian Guo[b], Jiajia Wang[a], Huan Pang[b,*]

[a] *Guangling College, Yangzhou University, Yangzhou 225009, China*
[b] *School of Chemistry and Chemical Engineering, Yangzhou University, Yangzhou 225009, China*

ARTICLE INFO

Article history:
Received 4 August 2022
Revised 5 September 2022
Accepted 14 September 2022
Available online 17 September 2022

Keywords:
Hierarchical structure
Nanosheets@nanorods
Electrocatalyst
NiO
Urea electrooxidation

ABSTRACT

Hierarchical NiO nanosheets@nanorods have been rationally designed and constructed for efficient urea electrooxidation in an alkaline solution. The critical synthetic strategy, engaging the one-step anion-competitive reaction, precisely integrates two nickel-based materials into a heterostructure with $Ni(OH)_2$ nanosheets and NiC_2O_4 nanorods. Benefiting from the hierarchically porous structure and high specific surface area, the NiO NNs can improve the escape efficiency of gas in electrochemical reactions and maintain sustainability. Furthermore, this distinctive structure can expose highly dispersed active sites for enhancing urea molecules' adsorption, surface-dependent redox reactions, and electrical conductivities. As a result, these hierarchical NiO nanosheets@nanorods exhibit superior activity with a low overpotential of 156 mV at 10 mA/cm^2, and a slight Tafel slope of 40.7 mV/dec, and high stability with almost no decay of 12,000 s for urea electrooxidation. This work promotes the application of well-designed hierarchical structure in electrooxidizing urea and provides a possibility for highly efficient electrolysis of alkaline urea wastewater.

Hierarchical nanostructures possess the apparent structural virtues over their ordinary single counterparts such as accessible and connected porous constructions, high content of exposed active sites, and the exquisite molecular structure is beneficial to the study of growth mechanism and the extendable design of catalyst [1,2]. Moreover, as the composition and complex hierarchically nanocomposites are highly related to their electrochemical properties, rational design of hierarchical nanostructures has attracted interest. Different from the traditional methods of regulating metal ions and ligand types, the design of hierarchical nanostructures has attracted special attention in recent years [3,4]. Concretely, the nanosheets@nanorods hierarchical architectures possess shortened electron transport path, large surface area and high stability, which will speed up transmission between species, improve reactant capture/adsorption, and promote reaction dynamics [5,6]. Therefore, construction of nanosheets@nanorods hierarchical catalysts is an effective strategy to improve the catalytic properties. For example, Lou *et al.* reported that a hierarchical double-shelled structure could expose abundant active sites, remarkably enhancing gas adsorption and surface-dependent redox reactions [7]. Hierarchical structures with various morphologies also showed outstanding durability through the continuous formation and release of gaseous catalytic products [8–11].

Currently, the endless demands for energy have caused a series of problems about energy depletion and environmental pollution [12–14]. Seriously, urea-rich wastewater may be discharged into nature through industrial and agricultural production, and scientific development of technology can make urea, a small organic molecule with hydrogen content up to 6.67 wt%, turn waste into treasure [15–17]. Besides, hydrogen fuel, regarded as one of most promising energy resource, has been valued most by its high-effect and environment friendly [9]. Notably, in many urea-involved energy devices, including urea electrolysis, photoelectrochemical urea splitting and direct urea fuel cells, the urea oxidation reaction (UOR) come to the spotlight recently as promising semi-reaction [10,16]. Moreover, UOR has been referred to as an attractive alternative to oxygen evolution reaction (OER) due to its much lower theoretical overall voltage (0.37 V *vs.* RHE), faster reaction rates, and safer hydrogen production [18–20]. However, similar to the high thermodynamic barriers of OER, UOR is hampered mainly by the slow 6 electron transfer process [21–23]. To promote the development of urea energy conversion, developing efficient UOR electrocatalytic materials is highly impending.

---

* Corresponding authors.
E-mail addresses: 060083@yzu.edu.cn (Q. Li), panghuan@yzu.edu.cn (H. Pang).

https://doi.org/10.1016/j.cclet.2022.107831

Recently, Ni-based catalysts possess invincible electrocatalytic performance for UOR. Among them, nickel oxide (NiO), regarded as a representative electrocatalyst for urea splitting due to its high efficiency in converting into the active site of NiOOH, has been well-studied as promising candidate [24–26]. However, for undesigned NiO, most of the metal active sites are enclosed firmly inside the materials and they are hard to release into the alkaline electrolyte, resulting in the dismal sustainability of UOR catalytic activity [27–29]. To address the above issue, extensive efforts have been devoted to searching for strategies to modify NiO. Besides the hierarchical well-designed structure construction, techniques including material surface structure design, electronic properties optimization, and metal substitution, have been demonstrated to improve the intrinsic activity of NiO [8,30–33]. For example, doping metal or nonmetal elements has been proved as an acceptable way to boost the catalytic performance of NiO [34–36]. Thus, it is highly satisfying to integrate this thinking into a design idea to improve the UOR performance of NiO.

Herein, we have demonstrated a facile hexamethylenetetramine (HMT)-hydrolytic coprecipitation-oxidation strategy to fabricate hierarchical structure NiO nanosheets@nanorods (NNs) as electrocatalysts for UOR (Scheme S1 in Supporting information). First, uniform $NiC_2O_4 \cdot 2H_2O$ nanorods (NRs) are synthesized through a regulated hydrothermal temperature-assisted method. Next, $NiC_2O_4 \cdot 2H_2O$ NRs are partially converted into hierarchical $Ni(OH)_2$ nanosheets (NSs) by a controlled hydrothermal heating process. Subsequent oxidization treatment of the as-obtained $Ni(OH)_2@NiC_2O_4 \cdot 2H_2O$ by thermal annealing in air leads to hierarchical NiO NNs. Consequently, the porous hierarchical NiO NNs with nonmetal elements doped can catalyze the urea with excellent activity and high durability. The resultant N-NiO/C-2 NNs electrocatalyst delivers outstanding activity and cycling property in alkaline of urea electrolyte for UOR. Specifically, it only needs an overpotential of 156 mV at 10 mA/cm^2 and exceptional stability (almost no decay after 12,000 s at 10 mA/cm^2).

The synthetic procedure of $Ni(OH)_2@NiC_2O_4$ NNs as precursors is depicted in Fig. 1a. First, HMT, which acts as the shape-directing agent at low temperature (40 °C), is used to modulate the growth of NiC_2O_4 NRs. Field-emission scanning electron microscopy (FESEM) image (Fig. 1b) shows that the obtained NiC_2O_4 NRs are uniform nanorods with distribution and smooth surface. The sharp peaks in the X-ray diffraction (XRD) pattern in Fig. 1i indicate the successful synthesis of NiC_2O_4 NRs (PDF#01–0299). A controlled hydrothermal treatment (90 °C) of the HMT leads to the formation of OH^-, which can react with Ni^{2+}, and form a competitive reaction with the $C_2O_4{}^{2-}$. The SEM images in Fig. 1c show that uneven nanosheets are formed on the surface of nanorods. The XRD pattern (Fig. 1i) shows two prominent peaks at around 9.7 and 22.6, which is consistent with the characteristic peak of α-$Ni(OH)_2$. In comparison to NiC_2O_4, $Ni(OH)_2$ is successfully detected in $Ni(OH)_2@NiC_2O_4$ NNs after the competitive anion reaction [37,38]. According to the SEM and Transmission electron microscopy (TEM) images (Fig. 1d), the nanorods have been entirely covered by lamellar aggregates around them, forming the hierarchical structure $Ni(OH)_2@NiC_2O_4 \cdot 2H_2O$ NNs after 4 h of hydrothermal reaction, which is similar to that of the sample reacting 2 h. When the reaction time is 4 h, the content of α-$Ni(OH)_2$ increases obviously, which can be attributed to the continuous generation of OH^- in the system with the constant hydrolysis of HMT, and thus steals a large amount of Ni^{2+} in the system $Ni(OH)_2$. Moreover, it can be observed in Fig. 1c that the nanosheet and nanorods in the composite demonstrate a tight binding, indicating that OH^- in the system can also partially transform NiC_2O_4 into $Ni(OH)_2$. Fourier transformed infrared spectra in Fig. S1 (Supporting information) further confirms the formation of $Ni(OH)_2@NiC_2O_4$ NNs after the HMT-hydrolytic coprecipitation reaction [37,39]. The above experiments and analysis show that the precursor nanomaterial $Ni(OH)_2@NiC_2O_4$ with consistent morphology can be prepared by designing suitable synthesis temperature and time.

To verify the extensibility of the synthesis strategy in the preparation of composite materials with the hierarchical structure, the same synthesis process is used to conduct co-precipitation reaction in Co^{2+} and Cu^{2+} aqueous solutions with HMT participation, respectively. $Co(OH)_2@CoC_2O_4$ and $Cu(OH)_2@CuC_2O_4$ composites with the hierarchical structure are successfully prepared. As shown in Fig. 1e, the morphology of the samples is that many dispersed flower-like aggregates grow on nano-sheet sums. These self-assembled flower spheres are distributed on the nanosheets supports with distinct layers, and constructed hierarchical structure (Fig. 1f). Further, the XRD pattern of the obtained sample (Fig. 1j) shows an unobtrusive peak at around 10°, which is consistent with the characteristic peak of $Co(OH)_2$ (PDF#51–1731). All obvious diffraction peaks can be indexed to the phase of CoC_2O_4 (PDF#01–0296). The morphologies of the $Cu(OH)_2@CuC_2O_4$ composites with hierarchical structure (nanosheets@nanoparticles) are illustrated in Figs. 1g and h. XRD pattern of the composites (Fig. 1k) can be assigned to the phases of $Cu(OH)_2$ (PDF#13–0420) and CuC_2O_4 (PDF#21–0297), indicating the synthetic methods can be extended to copper- based materials.

Combined with the analysis of thermogravimetric curves (Fig. S2 in Supporting information), $Ni(OH)_2@NiC_2O_4 \cdot 2H_2O$ NNs are annealed at different temperatures in the air, which are converted to NiO NNs. As shown in Fig. S3a (Supporting information), the sharp peaks attributed to (111), (200), (220) and (311) crystal facets in the XRD pattern can be well indexed to the NiO phase (PDF#71–1179), and the broad diffraction peak around 10° indicates the amorphous C element doping. X-ray photoelectron spectroscopy (XPS) analysis is further conducted to study the surface chemical states of NiO NNs. The survey spectrum in Fig. S3b (Supporting information) reveals the presence of Ni, O, C and N elements in the prepared samples. The XPS analysis of Ni 2p (Fig. S3c in Supporting information) suggests that there are two spin-orbit peaks, corresponding to Ni $2p_{1/2}$ at 870.0, 871.7 eV and Ni $2p_{3/2}$ at 852.7, 854.5 eV, confirming the superiority of Ni^{2+} [40–42]. The O 1s spectrum (Fig. S3d in Supporting information) can be subdivided into two peaks, the peak at 528.3 eV corresponding to the Ni–O bonds, and the peak at 530.1 eV attributed to the surface adsorbed H_2O. The peak-fitting analysis of the N 1s spectrum (Fig. S4 in Supporting information) shows two peaks, mainly at 399.1 and 401.5 eV, corresponding to the Ni–N bonds and surface oxidized N–O bonds, respectively. As revealed by the above results, the main composition of the prepared samples is NiO doped with non-metallic C and N elements [43–45].

To probe the morphology characteristic of the three samples obtained at different calcination temperatures (400, 450 and 500 °C), SEM and TEM images (Fig. S5 in Supporting information) are conducted. For comparison, $Ni(OH)_2@NiC_2O_4 \cdot 2H_2O$ NNs are also prepared as the reference. Figs. S5a1-a3 show that the as-prepared $Ni(OH)_2@NiC_2O_4 \cdot 2H_2O$ NNs are multistage structural characteristics of nanosheets grown *in situ* on nanorods. After a calcination treatment (400 °C, 2 h), the nanosheets edges of sample N-NiO/C-1 shrink with the appearance of pores, and uneven holes are distributed at the edge of the nanosheet in Figs. S5b1-b3. Notably, significant shrinkage of the overall size of the sample can be observed. When the calcination temperature is 450 °C, it can be observed in Fig. S5c1 that the nanorods grown on the surface of N-NiO/C-2 sample begin to shrink comprehensively (Fig. S5c2) and eventually appear uniformly distributed holes in the nanorods (Fig. S5c3). However, the multistage structure of the sample is consistent with that of the precursor. It is observed in Fig. S5d1 that the flake shrinkage and fragmentation on the surface of N-NiO/C-3

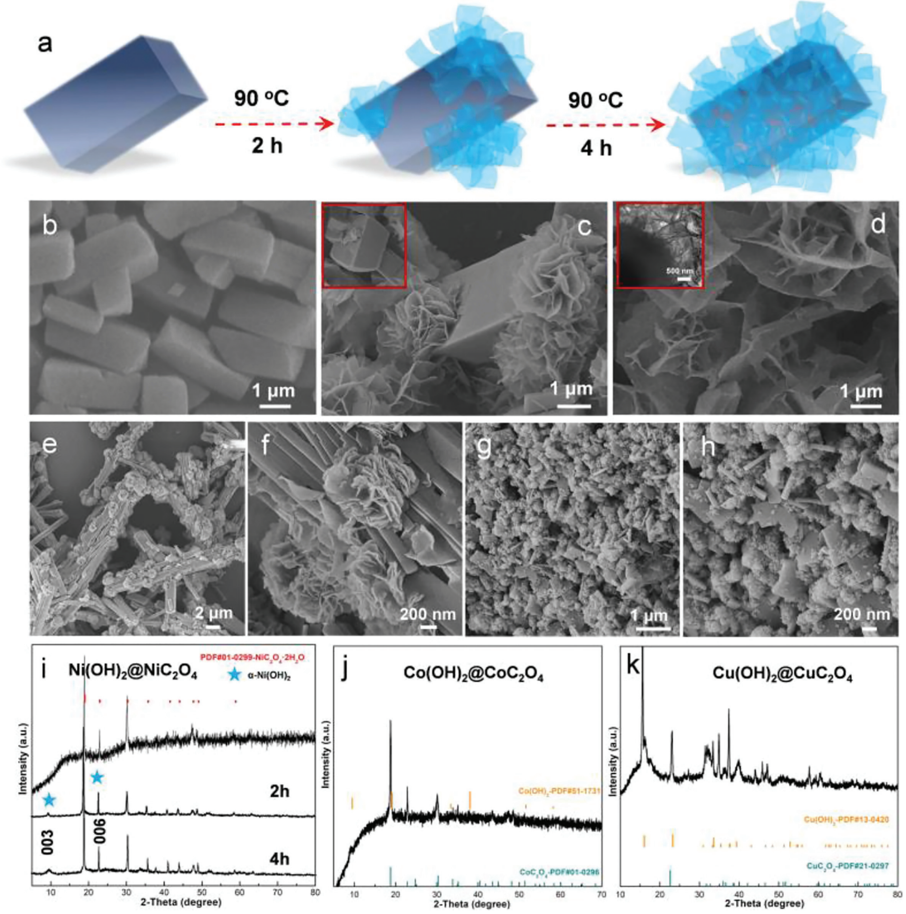

Fig. 1. (a) Schematic illustration of synthetic process of $Ni(OH)_2@NiC_2O_4$. (b-d) SEM images of $NiC_2O_4·2H_2O$, $Ni(OH)_2@NiC_2O_4·2H_2O$ (2 h) and $Ni(OH)_2@NiC_2O_4·2H_2O$ (4 h). (e-h) SEM images of $Co(OH)_2@CoC_2O_4$ and $Cu(OH)_2@CuC_2O_4$. (i) XRD patterns of $NiC_2O_4·2H_2O$, $Ni(OH)_2@NiC_2O_4·2H_2O$ (2 h) and $Ni(OH)_2@NiC_2O_4·2H_2O$ (4 h). (j) XRD patterns of $Co(OH)_2@CoC_2O_4$. (k) XRD patterns of $Cu(OH)_2@CuC_2O_4$.

resulted in the exposed nanorods wrapped inside at 450 °C As revealed by Fig. S5d2, the collapse and fragmentation of the flake structure can be observed. Even, the holes on the nanosheets are of different sizes and are not evenly distributed in Fig. S5d3. As revealed by the above results, the obtained samples can retain the original hierarchical structure after different temperatures treatment. The micromorphology of obtained samples by calcination at different temperatures is different, such as uniform pore distribution and pore size of multistage morphology. Therefore, the N-NiO/C-2 has a stable regular hierarchical structure, evenly distributed pores, and a uniform pore size, which can promote the adsorption of urea molecule and OH^- in the reaction system and provide an open channel for charge transfer of various gas products.

After the 450 °C annealing treatment in air, $Ni(OH)_2@NiC_2O_4·2H_2O$ NNs are converted to N-NiO/C-2 NNs. SEM and TEM images of N-NiO/C-2 NNs show that the NN morphology is well maintained, and a hollow interior can be observed from the processed NN (Figs. 2a-c). The well-defined NN structure with a straightforward interface and porous characteristics facilitates the exposure of more active sites. It benefits the release of gaseous products in UOR, which can be further observed in Figs. 2c and d. The N_2 sorption measurement further indicates that the N-NiO/C-2 NNs possess a mesoporous structure (2–10 nm) with the highest specific surface area of about 157.8 m^2/g compared to the N-NiO/C-1 (111.3 m^2/g) and N-NiO/C-3 (84.5 m^2/g) in Fig. S6 (Supporting information). The high-resolution TEM (HRTEM) images of the light and dark regions of N-NiO/C-2 NNs show corresponding lattice fringes in Fig. 2d. The clear lattice fringes with an interplanar distance of 0.21 nm (Fig. 2e), which can be ascribed to the (200) plane of the NiO nanorods (Fig. 2f), indicating its polycrystalline nature. The interplanar spacings of 0.24 nm (Fig. 2g), are

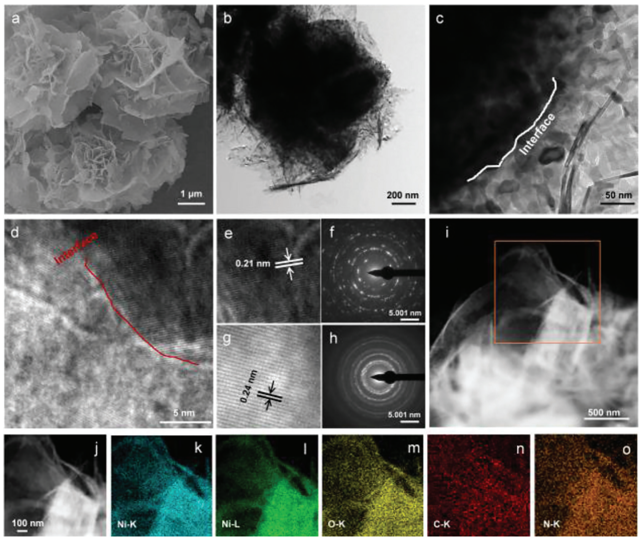

Fig. 2. N-NiO/C-2 NNs: (a) SEM, (b) TEM, (c, d) HRTEM and (e-h) SAED images at different magnifications. (i-o) Images of element distribution.

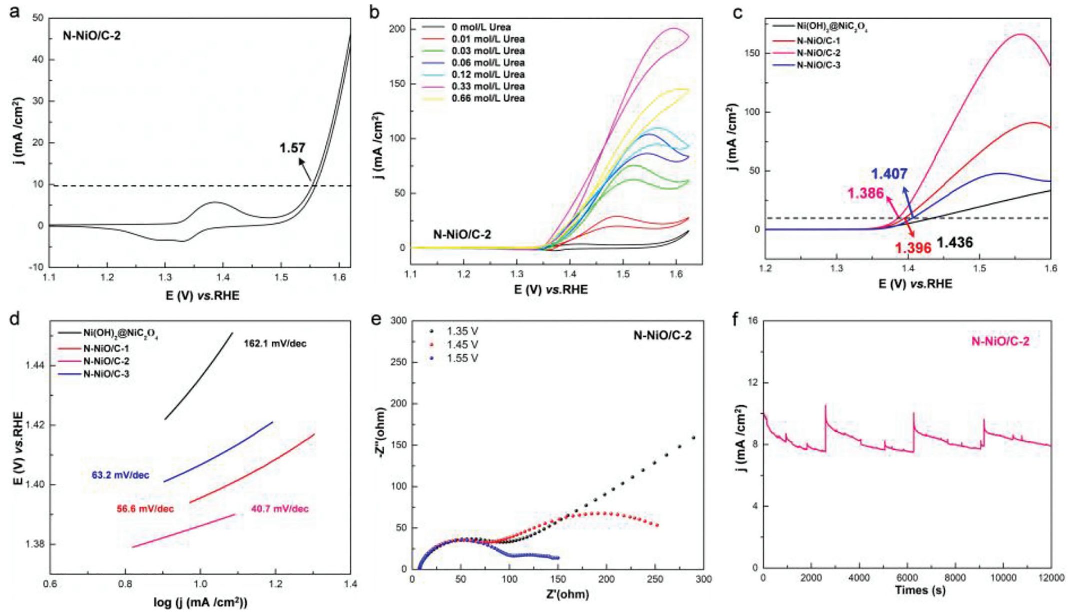

Fig. 3. Electrochemical studies. N-NiO/C-2 NNs (a) CV curves in 1 mol/L KOH. (b) CV curves at different concentrations urea solutions. (c) The LSV curves of four samples in 1 mol/L KOH + 0.33 mol/L urea. (d) Corresponding Tafel plots. (e) The electrochemical impedance spectra of N-NiO/C-2 NNs at different potentials. (f) The *i-t* curve under a static overpotential.

readily assigned to the (111) plane of NiO nanosheets. The corresponding SAED image (Fig. 2h) shows diffraction rings, revealing that NiO nanosheets have polycrystalline properties. The elemental mapping image shows the uniform distribution of Ni, O, C and N elements in N-NiO/C-2 NNs (Figs. 2i-o). The contents of C and N elements in the above NiO NNs are determined by an elemental analyzer, as shown in Fig. S7 (Supporting information). It can be speculated that C and N elements may be absorbed in obtained samples by the decomposition of HMT and NiC_2O_4. This unique configuration and diversity of exposed crystal faces endow the N-NiO/C-2 NNs with affluent active sites for UOR.

To reveal the advantages of the N-NiO/C-2 NNs, the electrochemical UOR measurements were carried out in the alkaline solution of urea (1 mol/L KOH + 0.33 mol/L urea) using a standard three-electrode system, with $Ni(OH)_2@NiC_2O_4 \cdot 2H_2O$ NNs, N-NiO/C-1 NNs and N-NiO/C-3 NNs as references. Fig. S8 (Supporting information) reveals the cyclic voltammetry (CV) curves of the three catalysts and the precursor of $Ni(OH)_2@NiC_2O_4 \cdot 2H_2O$ NNs. A broad redox peak is observed in all samples starting at around 1.35 V relative to the reversible hydrogen electrode (RHE) in 1 mol/L KOH, which is assigned to the oxidation of $Ni(OH)_2$ to NiOOH in Fig. S8a. Moreover, a significantly increased current density at about 1.5 V can be assigned to OER, and 10 mA/cm^2 can be obtained at 1.57 V (*vs.* RHE). To further understand the UOR potential range, it can be observed in Fig. S8b that the N-NiO/C-2 NNs catalyst shows a remarkably higher current density than the other three samples. In the case of 1 mol/L KOH+0.33 mol/L urea, the reduction peak is almost not observed in the CV curve, which is attributed to the large consumption of NiOOH by urea molecules. However, due to the occurrence of UOR, the oxidation current density of the sample increased significantly, presenting a noticeable degree of strength differentiation: N-NiO/C-2 > N-NiO/C-1 > N-NiO/C-3 > $Ni(OH)_2@NiC_2O_4$. Therefore, the potential range can be considered 1–1.57 V (*vs.* RHE), as shown in Fig. 3a, to investigate the UOR performance. Fig. 3b shows the UOR effect of urea solution with different concentrations on the N-NiO/C-2 NNs. Concretely, when urea concentration was 0–0.33 mol/L, the potential shifted to the right, and the overall oxidation current density increased. With the increase of urea concentration, the oxidation potential of the reaction shifts, which can be explained by Nernst equation. Specifically, when urea concentration increases, the theoretical electrode potential of electrochemical reaction will increase. When the concentration increased to 0.66 mol/L, the current density decreased owing to the saturation of urea molecules on the electrode surface. At low concentrations of 0.01 and 0.03 mol/L, the peak current density decreased at high potential (>1.5 V, *vs.* RHE), which can be attributed to insufficient urea molecules diffused on the electrode surface. Therefore, the optimal urea concentration of N-NiO/C-2 NNs is 0.33 mol/L urea in 1 mol/L KOH alkaline solution.

Fig. S9 (Supporting information) represents the linear sweep voltammetry (LSV) curves of the four electrodes in 0.33 mol/L urea, 1 mol/L KOH and 1 mol/L KOH + 0.33 mol/L urea solution, respectively. Almost no response is observed in 0.33 mol/L urea solution. The current signal increases obviously with the change of potential, which is attributed to the conversion of Ni^{2+} to Ni^{3+} on the electrode surface in 1 mol/L KOH. The negative electrode potential changes from 1 mol/L KOH solution to 1 mol/L KOH + 0.33 mol/L urea solution are 135, 176, 191 and 174 mV. Except for $Ni(OH)_2@NiC_2O_4$, the corresponding peak current densities of the other three samples are 91.2, 167.1 and 47.9 mA/cm^2. It is found that the N-NiO/C-2 NNs show the best UOR performance. From the LSV curves shown in Fig. 3c, the N-NiO/C-2 NNs offer better performance toward UOR with the lowest potential at the same current density of 10 mA/cm^2. Specifically, only a tiny overpotential of 156 mV is required for N-NiO/C-2 NNs to 10 mA/cm^2 (Table S1 in Supporting information), clearly outperforming N-NiO/C-1 NNs (166 mV), N-NiO/C-3 NNs (177 mV), and $Ni(OH)_2@NiC_2O_4$ NNs (206 mV). Moreover, the current density of N-NiO/C-2 NNs could reach 160.3 mA/cm^2 at 1.53 V, which is much higher than that of the others at the same potential (82.5, 47.7 and 24.2 mA/cm^2). This indicates high UOR efficiency for N-NiO/C-2 NNs relative to the others. The Tafel plots of the four catalysts are further estimated based on the LSV curves. As shown in Fig. 3d, the N-NiO/C-2 NNs exhibit enhanced UOR kinetics with the lowest Tafel slope of 40.7 mV/dec compared with 56.6 mV/dec (N-NiO/C-1 NNs), 63.2 mV/dec (for N-NiO/C-3 NNs)

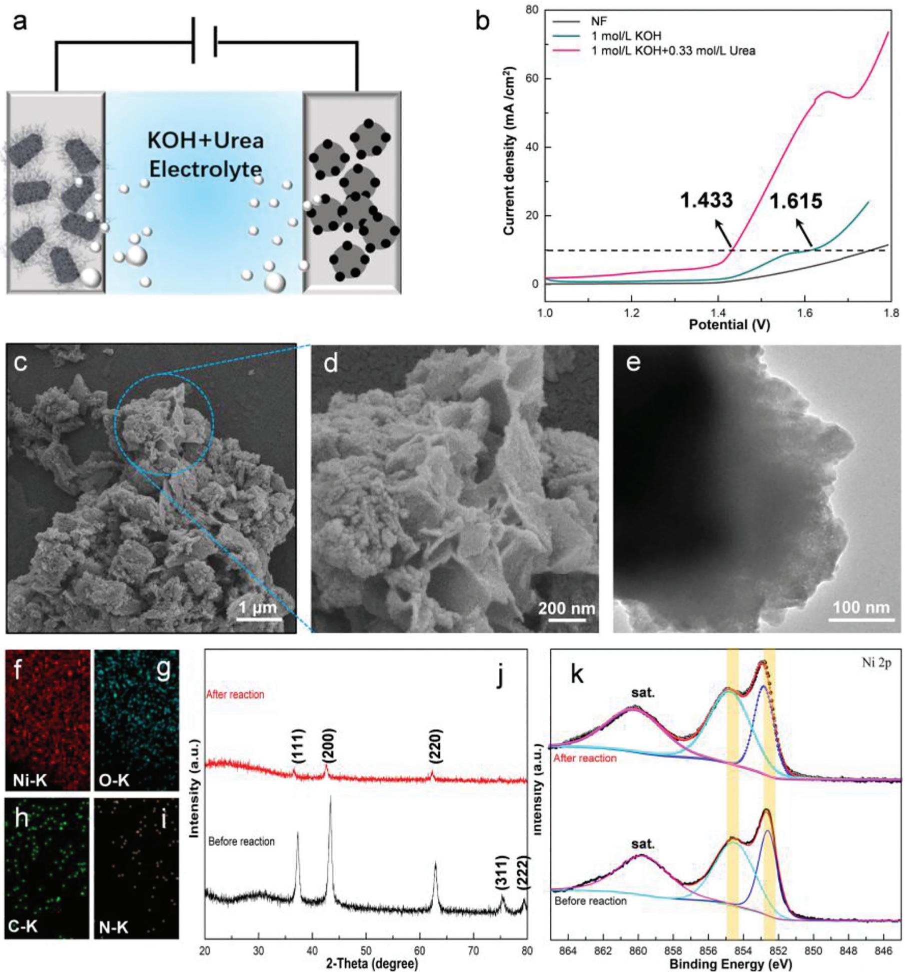

Fig. 4. (a) The diagram of overall urea electrolysis model. (b) Polarization curves of the two-electrode systems with Pt/C||N-NiO/C-2 electrode. Characterization after the cycling test: (c-e) SEM images and TEM image. (f-i) Element mapping. (j, k) XRD patterns and XPS spectra of Ni 2p.

and 162.1 mV/dec ($Ni(OH)_2@NiC_2O_4$ NNs) Electrochemically active surface area (ECSA) of electrode materials in UOR can be calculated by using the principle of the double-layer capacitance (C_{dl}). The CVs at scan rates from 5 mV/s to 100 mV/s are tested in the voltage range of 1.02–1.12 V, while the N-NiO/C-2 NNs reveal the highest *C*dl of 5.22 mF/cm^2 (Fig. S10 and Table S3 in Supporting information). The electrochemical impedance of N-NiO/C-2 NNs at different potentials is further analyzed to evaluate the UOR kinetics (Fig. 3e). The result indicates that N-NiO/C-2 NNs have promoted UOR charge transfer ability. Besides the catalytic activity, the electrochemical stability is also evaluated through measurement (Fig. 3f), in which N-NiO/C-2 NNs demonstrate substantial durability. Hence, the N-NiO/C-2 NNs, which possess a low overpotential, continuous stability, and fast current density rise, reflects the importance of porous hierarchical nanostructure and nonmetal elements doping for enhancing the UOR properties.

To further assess the electrocatalytic properties of the hierarchical N-NiO/C-2 NNs in the same alkaline urea electrolyte for overall urea electrolysis was constructed with a two-electrode cell (Fig. 4a). The current density of 10 mA/cm^2 is reached at 1.433 V compared to 1.615 V in 1 mol/L KOH (Fig. 4b). Besides, the two-electrode cell shows good stability, with about 82.0% of the initial current density retained after the stability test of 12000 s (Fig. S11 in Supporting information). The UOR activity and stability of N-NiO/C-2 NNs also compared with those of electrocatalysts (Table S2 in Supporting information). Moreover, the FESEM and TEM images of the N-NiO/C-2 NNs in Figs. 4c-e after the CV test for 2000 cycles reveal that the hierarchical NNs structure is preserved. However, the outer layer of the nanosheets thickens, which might be induced by the transformation of the NiO on the surface into amorphous NiOOH during the UOR. This tentative can be proved by the XRD and XPS after cycling observation (Figs. 4j and k).

Considering the excellent enhancement of UOR performance, we performed a hypothesis to reveal the mechanism of as-prepared N-NiO/C-2 NNs during the UOR process: (1) Hierarchical NiO NNs constructed with distributed mesoporous pores and large specific surface area can form $Ni(OH)_2$ owing to the adsorption large quantities of OH^- and urea molecules in the electrolyte. (2) The apparent redox peaks at about 1.32 V *vs.* RHE can be assigned to the oxidation of $Ni(OH)_2$ to NiOOH, indicating that the surface of NiO NNs undergoes redox transitions before the occurrence of UOR. It can be observed that the N-NiO/C-2 NNs still maintained the original morphological and structural characteristics. Only the layered nanosheets become rough, which is conducive to the continuous exposure of the active site (Figs. 4c-e). Concretely, more and more NiOOH is enriched in the surface interface of the nanosheets with the increase of potential. XRD patterns after testing compared with the before, the (311) and (222) crystal plane of NiO almost disappeared. In comparison, the diffraction peak intensity of the detected (111) and (200) crystal plane become weak and shifted, which indicates the formation of amorphous form the crystalline surface in Fig. 4j. Moreover, Ni $2p_{3/2}$ turned to a higher binding energy direction and widened, indicating the formation of Ni^{3+} on the surface of nanomaterials after cyclic testing (Fig. 4k). The content of the O element in the sample increases significantly after the long-term UOR, mainly due to the generation of $Ni(OH)_2$ and NiOOH species during the UOR (Figs. 4f-i). (3) At 1.386 V *vs*. RHE, a sufficient amount of NiOOH is generated, and $CO(NH_2)_2$ is oxidized. Based on the high efficiency of the NNs structure in adsorbing and desorbing gas, high-efficiency UOR is continued at 1.53 V *vs*. RHE, and the current density can reach 160.3 mA/cm^2.

In summary, we demonstrate that hierarchical structure NiO nanosheets@nanorods (N-NiO/C NNs) as an electrocatalyst exhibit remarkable activities for UOR. Starting from the NiC_2O_4 nanorods, hierarchical precursor $Ni(OH)_2@NiC_2O_4$ NNs are first obtained by using HMT as both nitrogen and alkali sources. Subsequently, hierarchical structure NiO NNs doped with nitrogen and carbon are formed through annealing treatment in air. The ultrathin nanosheets and hierarchical structure can expose plentiful active sites and facilitate a significant increase in stability. Importantly this synthesis can be applied to the preparation of Cu-based and Co-based hierarchical structure species. The obtained N-NiO/C NNs have dramatically enhanced the intrinsic electroactivity of the UOR. Significantly, the as-prepared N-NiO/C NNs show remarkable catalytic activity toward UOR with an overpotential of 156 mV to reach the current density of 10 mA/cm^2, a small Tafel slope of 40.7 mV/dec, and exhibits excellent stability. This work may provide an insight into the design of a rational Ni-based UOR electrocatalyst with hierarchical structure, whose composition, interconnected porous organization, and morphology features could be exquisitely designed.

Declaration of competing interest

The authors declare that they have no known competing financial interests or personal relationships that could have appeared to influence the work reported in this paper.

Acknowledgments

This work was supported by the National Natural Science Foundation of China (No. U1904215), Natural Science Foundation of Jiangsu Province (No. BK20200044), Program for Young Changjiang Scholars of the Ministry of Education, China (No. Q2018270). We also acknowledge the Priority Academic Program Development of Jiangsu Higher Education Institutions, Natural Science Research Project of Guangling College, Yangzhou University (No. ZKZD22004). and the technical support we received at the Testing Center of Yangzhou University.

Supplementary materials

Supplementary material associated with this article can be found, in the online version, at doi:10.1016/j.cclet.2022.107831.

References

[1] X. Jiao, X. Li, X. Jin, et al., J. Am. Chem. Soc. 139 (2017) 18044–18051.
[2] W. Yang, L. Zhang, J. Xie, et al., Angew. Chem. Int. Ed. 55 (2016) 6716–6720.
[3] G. Zhan, H.C. Zeng, Nat. Commun. 9 (2018) 3778.
[4] C. Liu, Q. Sun, L. Lin, et al., Nat. Commun. 11 (2020) 3680–3686.
[5] M. Fang, G. Dong, R. Wei, J.C. Ho, Adv. Energy Mater. 7 (2017) 1770135.
[6] Y. Zhao, X. Jia, G. Chen, et al., J. Am. Chem. Soc. 138 (2016) 6517–6524.
[7] L. Yu, X.Y. Yu, X.W.D. Lou, Adv. Mater. 30 (2018) 1800939.
[8] J. Liu, J. Zhang, Chem. Rev. 120 (2020) 2123–2170.
[9] S. Chen, Z. Kang, X. Hu, et al., Adv. Mater. 29 (2017) 1701687.
[10] B.Y. Guan, L. Yu, X.W. (David) Lou, J. Am. Chem. Soc. 138 (2016) 11306–11311.
[11] Y. Jia, L. Zhang, G. Gao, et al., Adv. Mater. 29 (2017) 1700017.
[12] S. Zheng, Y. Ru, H. Xue, H. Pang, Chin. Chem. Lett. 32 (2021) 3817–3820.
[13] W. Li, X. Guo, P. Geng, et al., Adv. Mater. 33 (2021) 2105163.
[14] Y. Bai, C. Liu, T. Chen, et al., Angew. Chem. Int. Ed. 60 (2021) 25318–25322.
[15] X. Zhu, X. Dou, J. Dai, et al., Angew. Chem. Int. Ed. 55 (2016) 12465–12469.
[16] C. Wang, H. Lu, Z. Mao, et al., Adv. Funct. Mater. 30 (2020) 2000556.
[17] Q. Zhang, F.M. Kazim, S. Ma, K. Qu, et al., Appl. Catal. B: Environ. 280 (2021) 119436.
[18] Y. Zhang, C. Wang, Chin. Chem. Lett. 32 (2021) 2222–2228.
[19] T. Li, H.C. Fu, X.H. Chen, et al., J. Colloid Interface Sci. 618 (2022) 196–205.
[20] A.N. Rollinson, J. Jones, V. Dupont, M.V. Twigg, Energy Environ. Sci. 4 (2011) 1216.
[21] C.B. Castro, R.G. Silveira, F.M. Colombari, et al., Chemistry 2 (2020) 525–544 (Easton).
[22] Q. Li, S. Zheng, M. Du, H. Pang, Chem. Eng. J. 417 (2021) 129201.
[23] L. Zhang, L. Wang, H. Lin, et al., Angew. Chem. Int. Ed. 58 (2019) 16820–16825.
[24] Y. Tong, P. Chen, M. Zhang, et al., ACS Catal. 8 (2018) 1–7.
[25] C. Alex, G. Shukla, N.S. John, Electrochim. Acta 385 (2021) 138425.
[26] J. Ge, Z. Liu, M. Guan, et al., J. Colloid Interface Sci. 620 (2022) 442–453.
[27] S. Zheng, Y. Zheng, H. Xue, H. Pang, Chem. Eng. J. 395 (2020) 125166.
[28] Z.Y. Yu, C.C. Lang, M.R. Gao, et al., Energy Environ. Sci. 11 (2018) 1890–1897.
[29] X. Ji, Y. Zhang, Z. Ma, Y. Qiu, ChemSusChem 13 (2020) 5004–5014.
[30] J. Zhang, F. Xing, H. Zhang, Y. Huang, Dalton Trans. 49 (2020) 13962–13969.
[31] W. Yan, D. Wang, L.A. Diaz, G.G. Botte, Electrochim. Acta 134 (2014) 266–271.
[32] Y. Liu, N.O. Weiss, X. Duan, et al., Nat. Rev. Mater. 1 (2016) 16042.
[33] J.L. Fenton, B.C. Steimle, R.E. Schaak, Science 360 (2018) 513–517.
[34] Q. Li, N. Li, J. An, H. Pang, Inorg. Chem. Front. 7 (2020) 2089–2096.
[35] P. Liu, J. Ran, B. Xia, et al., Nano-Micro Lett. 12 (2020) 68.
[36] S. Lu, Z. Gu, M. Hummel, Y. Zhou, et al., J. Electrochem. Soc. 167 (2020) 106509.
[37] H. Lai, Q. Wu, J. Zhao, et al., Energy Environ. Sci. 9 (2016) 2053–2060.
[38] S. Powar, Q. Wu, M. Weidelener, A. Nattestad, et al., Energy Environ. Sci. 5 (2012) 8896.
[39] J. Xiong, H. Shen, J. Mao, et al., J. Mater. Chem. 22 (2012) 11927.
[40] X. Xu, L. Li, J. Huang, et al., ACS Catal. 8 (2018) 8033–8045.
[41] L. Zhang, J.S. Hu, X.H. Huang, J. Song, S.Y. Lu, Nano Energy 48 (2018) 489–499.
[42] F. Zhang, R. Ji, Y. Liu, et al., Appl. Catal. B: Environ. 276 (2020) 119141.
[43] Y. Li, C. Xu, K. Liu, P. Chen, X. Gao, Nanomaterials 10 (2020) 1502.
[44] Y. Ni, Y. Yin, P. Wu, H. Zhang, C. Cai, ACS Appl. Mater. Interfaces 6 (2014) 7346–7355.
[45] S. Seok, D. Jang, H. Kim, S. Park, Carbon Lett. 30 (2020) 485–491.